

# Vehicle-to-Vehicle Millimeter-Wave Channel Characterization at 60 and 80 GHz

Radek Zavorka\*, Jiri Blumenstein\*, Tomas Mikulasek\*, Josef Vychodil\*, Hussein Hammoud†, Wojtuń Jarosław §, Aniruddha Chandra ‡, Markus Hofer ||, Jan M. Kelner §, Cezary Ziółkowski §, Christoph Mecklenbräuer ¶, Ales Prokes \*

\*Department of Radio Electronics, Brno University of Technology, Brno, Czech Republic

†University of Southern California, Los Angeles, USA

‡National Institute of Technology, Durgapur, India

§ Institute of Communications Systems, Military University of Technology, Warsaw, Poland

¶Institute of Telecommunications, TU Wien, Vienna, Austria

|| AIT Austrian Institute of Technology, Vienna, Austria

e-mail: xzavor03@vutbr.cz

**Abstract**—This paper presents results from a vehicle-to-vehicle channel measurement campaign conducted in the millimeter-wave (MMW) frequency bands at center frequencies of 60 GHz and 80 GHz, each with a bandwidth of 2 GHz. The measurements were performed in a dynamic oncoming-vehicle scenario using a time-domain channel sounder with high-resolution data acquisition. Power delay profiles were extracted to study the temporal evolution of multipath components, and the root mean square (RMS) delay spread was analyzed to characterize the temporal dispersion of the channel. The results demonstrate differences between the two frequency bands. At 60 GHz, the RMS delay spread is well approximated by a Gaussian distribution with a higher median value, while at 80 GHz it follows a lognormal distribution with a lower median. Furthermore, the number of resolvable multipath components was found to be nearly twice as high at 60 GHz compared to 80 GHz, highlighting the impact of antenna beamwidth and frequency-dependent propagation mechanisms.

**Index Terms**—millimeter-wave, vehicle-to-vehicle, RMS delay spread, statistical distribution, channel sounder

## I. INTRODUCTION

Vehicle-to-vehicle (V2V) communication in the millimeter-wave (MMW) bands is a key enabler of emerging intelligent transportation systems (ITSs) and autonomous driving, as it delivers the high data rates and low latency required for these applications [1]. This is achieved through the large bandwidth at MMW frequencies, which supports gigabit-per-second links for cooperative awareness and real-time sensor sharing between vehicles.

In addition, the shorter wavelength at these frequencies allows for compact antenna arrays with high beam-forming gain [2], thereby improving spatial selectivity and spectrum reuse. Despite these advantages, the propagation characteristics of V2V channels at MMW frequencies remain challenging. High path loss, susceptibility to blockage, and rapid temporal variations due to vehicle mobility all strongly impact link reliability.

Several measurement campaigns have been reported in the literature [3], [4], focusing on different frequencies

and scenarios within the MMW bands. The authors in [5] summarize results from multiple measurement campaigns carried out at 3.2 GHz, 34.3 GHz, and around 60 GHz for both V2V and vehicle-to-infrastructure (V2I) scenarios, showing that in all analyzed cases the root mean square (RMS) delay spread was below 100 ns. In [6], the authors report results from a V2V campaign conducted in an urban street canyon at a center frequency of 60 GHz with a bandwidth of 500 MHz. The power delay profile (PDP) was analyzed, and the study showed that a passenger car gives rise to a single multipath component, whereas a larger vehicle such as a truck produces several multipath components.

The influence of blockage was investigated in [7] at multiple frequency bands (6.75, 30, 60, and 73 GHz) in both urban and highway scenarios. The results show that blockage loss strongly depends on the blocker size, increasing from 5.5–8.2 dB for small blockers to 8.2–17 dB for large blockers. Furthermore, [8] presents dynamic vehicular integrated sensing and communication (ISAC) channel measurements at 28 GHz and introduces a tapped-delay line model that distinguishes between sensing multi-path components (S-MPCs) and clutter multi-path components (C-MPCs). An multipath component (MPC) distance (MCD)-based tracking algorithm is employed to statistically characterize lifetimes, power evolution, clustering, and fading of MPC, and the model is validated through comparison of measured and simulated results, confirming its suitability for vehicular ISAC system design.

### A. Contribution of the Paper

This paper presenting a dedicated V2V channel measurement campaign conducted at 60 GHz and 80 GHz with 2 GHz bandwidth. Using a time-domain channel sounder, we analyze PDP, characterize the RMS delay spread distributions, and study the temporal evolution of MPC in an oncoming-vehicle scenario. The results provide empirical evidence of frequency-dependent dif-

ferences between the two bands and highlight the importance of accurate, frequency-specific channel models for the design and evaluation of MMW vehicular communication systems.

The main contributions of this paper are as follows:

- Analysis of MPC propagating between two oncoming vehicles at two MMW frequency bands (60 GHz and 80 GHz), including their time-dependent statistical characterization.
- Evaluation and comparison of the RMS delay spread characteristics and their statistical distributions at both frequencies.
- Investigation of the temporal evolution in the number of propagation paths and evaluation of differences between frequency bands.

## II. MEASUREMENT CAMPAIGN DESCRIPTION

The measurement campaign focused on characterizing the high-mobility V2V channel in a real-world environment. Measurement was conducted on the campus of the Faculty of Electrical Engineering and Communication (FEEC), Brno University of Technology (BUT), Brno, Czech Republic, in the area between the T12 building on Technicka Street, the sports complex, and the adjacent parking lot. This location was selected because it combines open-space conditions with the presence of reflecting objects, creating a representative V2V environment. A visualization of the campaign, including the route and surrounding environment, is shown in Fig. 1. The studied scenario considered two vehicles approaching each other from opposite directions.

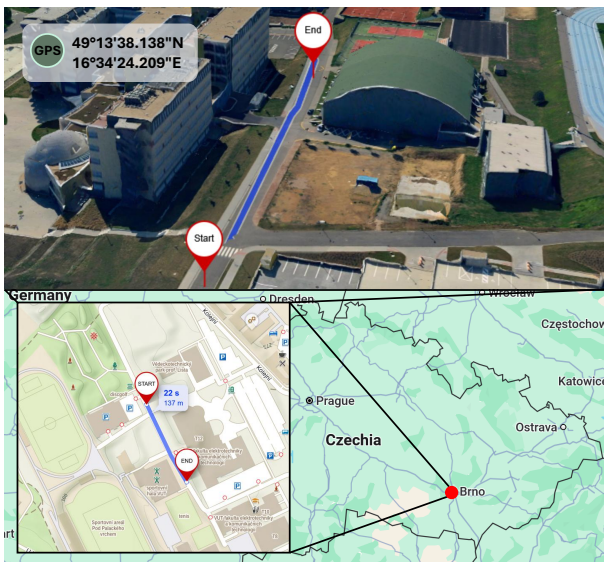


Fig. 1: Location of the measurement campaign with a detailed 3D view.

Along the road within the measurement area, several potential scatterers and reflectors were present, including parked cars, streetlights, traffic signs, medium-sized trees, and the nearby sports complex building. The pillars

and wall of the building were located approximately 3 m and 6.5 m from the road, respectively, with the wall reaching a height of 9 m. The road itself was approximately 6 m wide, with sidewalks of about 2 m on both sides.

Transmit and receive antennas with front-end units were mounted on the roofs of the vehicles, as illustrated in Fig. 2. The Skoda Eniaq carried both transmit antennas, with the 80 GHz unit positioned closer to the front of the car and the 60 GHz unit placed behind it toward the rear. The antennas were aligned at the same height, centered along the longitudinal axis of the vehicle, and separated by approximately 20 cm. The same configuration was applied at the receiver side, mounted on the second vehicle, a Skoda Superb III. The transmitter vehicle followed a trajectory from the defined start point to the end point at an average speed of about 45 km/h, while the receiver vehicle traveled in the opposite direction at a speed of approximately 35 km/h. The total channel impulse response (CIR) recording spanned 8 s, but for further processing only the most relevant 4 s segment with the highest signal-to-noise ratio (SNR) was selected.



Fig. 2: Vehicles equipped with antennas and front-end units on the roof for 60 and 80 GHz.

## III. MEASUREMENT SETUP

The transmit baseband section of the time-domain channel sounder was realized using the Xilinx Zynq UltraScale+ RFSoc ZCU111 platform. High-speed digital-to-analog converters (DAC) with a sampling rate of 6.144 GSPS generated the in-phase (I) and quadrature (Q) components of the intermediate-frequency signal. As a probing waveform, a frequency modulated continuous wave (FMCW) signal with both up- and down-chirp slopes was applied, ensuring a spectrum with minimal irregularities.

The main motivation for selecting an FMCW waveform was its robustness to system nonlinearities. With a bandwidth of  $B = 2.048$  GHz and a sweep duration of  $T = 8 \mu\text{s}$ , the waveform supports a high measurement rate of  $f_{\text{meas}} = 1/T = 125$  kHz (measurements per second), while still preserving a satisfactory SNR. In static measurement conditions, further improvement of the SNR can be achieved through averaging.

Upconversion to the target MMW bands was carried out using Siverts IMA converters, specifically the FC1005V/00 for 60 GHz and the FC1003E/03 for 80 GHz. A frequency-stable, low phase-noise local oscillator signal was supplied by an Agilent 83752A generator. The resulting radio frequency (RF) signal was subsequently amplified by a QuinStar QPW-50662330-C1 amplifier at 60 GHz or a Filtronic Cerus 4 AA015 amplifier at 80 GHz, and then transmitted through an omnidirectional antenna. The radiation patterns of the 60 GHz and 80 GHz antennas are shown in Fig. 3, and their detailed parameters are listed in Tab. I.

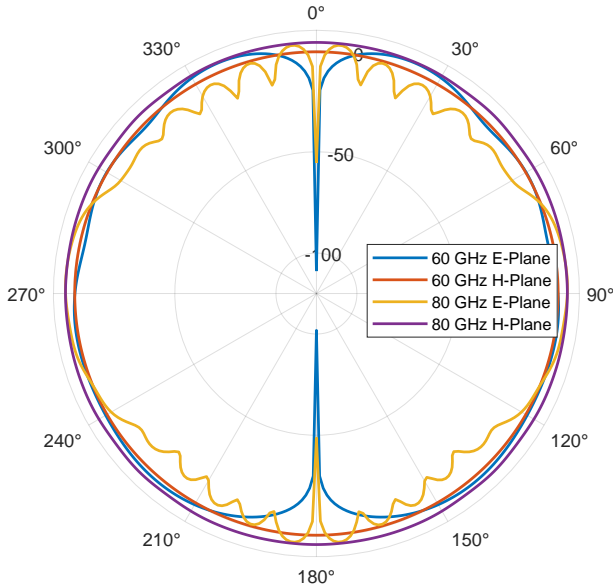


Fig. 3: Comparison of antenna radiation patterns in the E-plane and H-plane at 60 and 80 GHz.

TABLE I: Parameters of omnidirectional antennas at 60 and 80 GHz.

	60 GHz	80 GHz
Gain [dBi]	-0.3	3.7
HPBW E-plane [°]	156	40

On the receive side, the architecture mirrored that of the transmitter. The signal, captured by the same type of omnidirectional antenna, was first amplified using either a QuinStar QPW-50754530-I2 amplifier at 60 GHz or a Low Noise Factory *LNF-LNR55\_96WA\_SV* amplifier at 80 GHz. Downconversion was then carried out by a Siverts IMA FC1003V/01 (60 GHz) or FC1003E/02 (80 GHz) converter, driven by a local oscillator signal generated by an Agilent E8257D. The resulting intermediate-frequency signal, represented by its I and Q components, was digitized using high-speed analog-to-digital converters (ADCs) operating at 4.096 GSps on a second Xilinx Zynq UltraScale+ RFSoc ZCU111 board. The data were stored on a solid-state drive (SSD) for subsequent offline processing. Additional informa-

tion about the testbed, calibration procedure, and data processing for extracting the CIR can be found in [9].

#### A. High-Resolution Data Recording Principle

The measurement setup, based on the Xilinx Zynq UltraScale+ RFSoc ZCU111 board described above, enables high-resolution data acquisition. In each clock cycle, 256 bits (32 bytes) of data are captured, with every complex sample consisting of 4 bytes (16 bits for I and 16 bits for Q). This corresponds to 8 samples per cycle. Due to the large data volume, continuous recording over several seconds is not feasible for direct processing. Instead, the recording strategy is illustrated in Fig. 4. The acquisition window length was set to 262,144 samples, corresponding to 128  $\mu$ s. From each window, only the first 16,384 samples (equivalent to 8  $\mu$ s) were retained, while the remaining portion was discarded. To obtain a total duration of 8.4 s,  $M = 65,536$  windows were recorded, which required approximately 4.3 GB of storage.

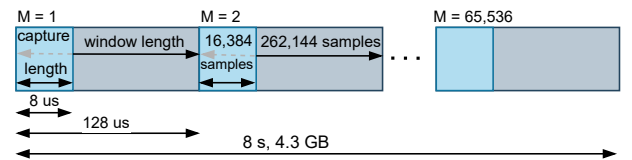


Fig. 4: Graphical representation of the high-resolution data recording principle.

## IV. STOCHASTIC CHANNEL CHARACTERIZATION

This section presents stochastic channel characterization based on empirical V2V channel measurements.

Our time-domain channel sounder was used to estimate the CIR, expressed as

$$h(t, \tau) = \sum_{n=1}^{N(t)} \alpha_n(t) \delta(\tau - \tau_n(t)), \quad (1)$$

where  $h(t, \tau)$  is the equivalent complex baseband CIR,  $N(t)$  is the number of propagation paths,  $\alpha_n(t)$  is the complex-valued path gain, and  $\delta$  represents the Dirac delta function. The power distribution across delayed propagation paths is described by the PDP, defined as

$$P(\tau) = \mathbb{E}\{|h(t, \tau)|^2\}, \quad (2)$$

where  $\mathbb{E}\{\cdot\}$  denotes the expectation taken over several realizations of CIRs.

The measured PDP of the passing vehicles is shown in Fig. 5a and Fig. 5b. The dominant line-of-sight (LOS) component is clearly visible, while the remaining MPCs originating from surrounding objects appear either in clusters or as isolated paths. In both cases, weak MPCs can be observed up to a distance of 80 m, which corresponds to a delay of 266.6 ns. To improve the visibility of relevant components, all values below the noise floor were discarded. A fixed threshold of  $-66$  dB

for the 60 GHz band and  $-65$  dB for the 80 GHz band was applied to suppress background noise. The use of different thresholds is attributed to slight differences in the measurement setup for each band, particularly in terms of dynamic range (40 dB at 60 GHz and 45 dB at 80 GHz). It should be noted that, despite careful calibration, small inconsistencies between the setups may still lead to variations in the observed MPCs in the PDP. In particular, the distinct antenna half power beam width (HPBW) in both bands ( $156^\circ$  at 60 GHz and  $40^\circ$  at 80 GHz) contributes to these differences.

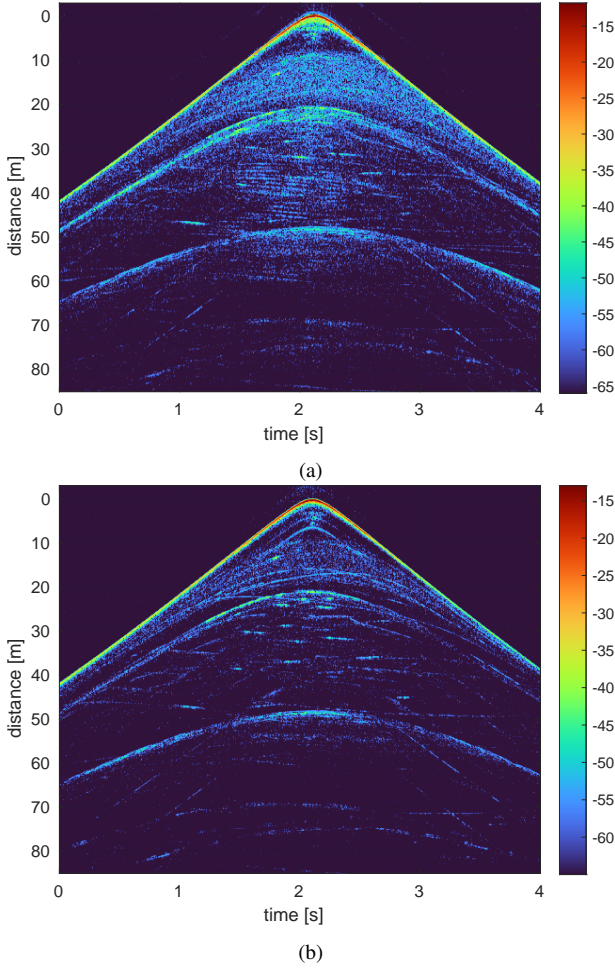


Fig. 5: Measured PDPs of passing vehicles for the 60 GHz (a) and 80 GHz (b) bands.

### A. Frequency and Time Dependence of RMS Delay Spread

The temporal dispersion of the radio channel is described by the RMS delay spread. This parameter quantifies the extent of multipath propagation, where distinct signal components travel over different paths and arrive at the receiver with varying delays. The RMS delay spread is defined as the square root of the second central moment of the PDP:

$$\sigma_\tau(t) = \sqrt{\overline{\tau^2(t)} - (\overline{\tau(t)})^2} \quad (3)$$

where  $\overline{\tau(t)}$  denotes the mean excess delay and  $\overline{\tau^2(t)}$  is the second moment of delay, both defined as

$$\overline{\tau(t)} = \frac{\sum_{n=1}^{N(t)} P(\tau_n, t) \tau_n(t)}{\sum_{n=1}^{N(t)} P(\tau_n, t)}, \quad (4)$$

$$\overline{\tau^2(t)} = \frac{\sum_{n=1}^{N(t)} P(\tau_n, t) \tau_n^2(t)}{\sum_{n=1}^{N(t)} P(\tau_n, t)}. \quad (5)$$

Here,  $P(\tau_n, t) = \mathbb{E}\{|h(t, \tau_n)|^2\}$  represents the PDP tap at the delay  $\tau_n$ ,  $N(t)$  is the number of multipath components at time  $t$ , and  $h(t, \tau_n)$  denotes the complex CIR at the delay  $\tau_n$  in time  $t$ .

The statistical distribution of the RMS delay spread over the measurement interval is shown in Fig. 6a, where the probability density function (PDF) for both frequency bands are depicted, while the corresponding cumulative distribution function (CDF) are presented in Fig. 6b. The PDF illustrates the relative likelihood of particular RMS delay spread values, whereas the CDF represents the probability that the spread does not exceed a given threshold. The results indicate that the two measured frequency bands exhibit distinct statistical behaviors. The distribution of the RMS delay spread at 60 GHz is well approximated by a Gaussian distribution, with the 50th percentile (median) equal to 19.97 ns. In contrast, the 80 GHz band is more accurately modeled by a lognormal distribution, with a corresponding median value of 16.71 ns.

$$F_{\sigma_\tau}^{60}(\tau_{50}^{60}) = 0.5, \quad \tau_{50}^{60} = 19.97 \text{ ns}, \quad (6)$$

$$F_{\sigma_\tau}^{80}(\tau_{50}^{80}) = 0.5, \quad \tau_{50}^{80} = 16.71 \text{ ns}, \quad (7)$$

where  $F_{\sigma_\tau}^{60}(\cdot)$  and  $F_{\sigma_\tau}^{80}(\cdot)$  denote the CDF of the RMS delay spread at 60 GHz and 80 GHz, respectively.

### B. Temporal Variation of Multipath Components

The complex propagation environment gives rise to a large number of MPCs between the transmitter and receiver. In realistic scenarios, the channel is inherently time-varying due to the motion of obstacles such as humans or vehicles. In our measurement campaign, the situation is even more dynamic since both the transmitter and the receiver were moving. As illustrated by the evolution of the PDP in Fig. 5a and Fig. 5b, the vehicles started approximately 42 m apart, approached each other, passed at around  $t \approx 2.1$  s, and then continued in opposite directions. Throughout the measurement, a strong LOS component was present. The number of resolvable MPCs varied over time  $t$  within each PDP, and additional fading effects were observed as a function of the propagation delay  $\tau_n$ . These variations were determined by the relative positions of the vehicles, surrounding objects, and multipath reflections from the environment.

From the analysis of the PDP, the number of resolvable propagation paths over time  $t$  was extracted for both frequency bands. Fig. 7(a) and Fig. 7(b) show the

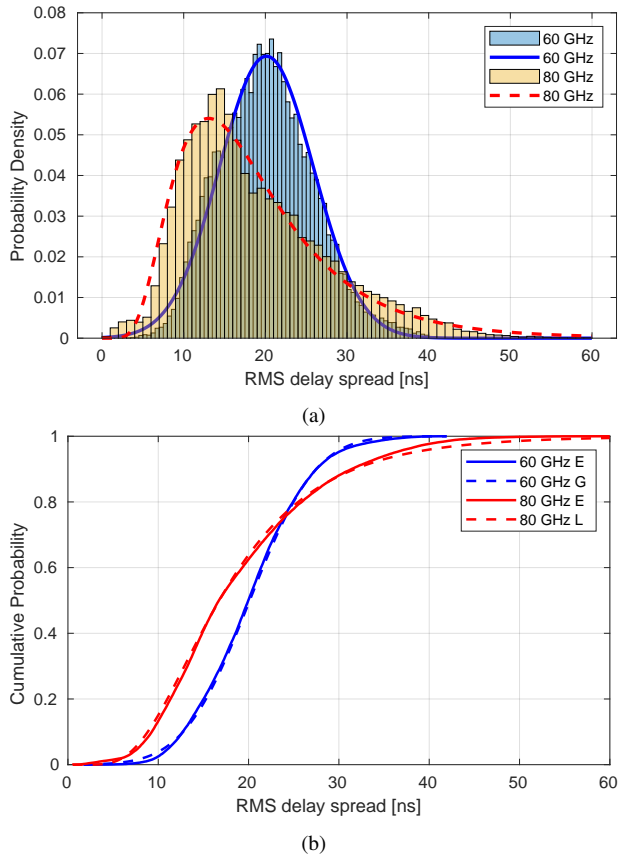


Fig. 6: Probability density function (a) and cumulative distribution function (b) of the RMS delay spread. Legend: Empirical (E), Gaussian (G), and Lognormal (L).

temporal variation and enable a comparison between the two bands. The overall shape of the curves reflects the scenario of two vehicles passing in opposite directions. At the beginning and end of the measurement, when the vehicles were relatively far apart, the number of resolvable paths was limited to about 10–20. As the vehicles approached each other, the number of paths increased almost linearly, reaching a sharp peak around  $t \approx 2.1$  s, and then decreased symmetrically as the vehicles moved away. The triangular shape of the curves highlights the strong dependence of multipath richness on the relative vehicle distance.

The 80 GHz band is characterized by more pronounced short-term fluctuations around the moving average (red line), with a variance of approximately 12 paths, compared to about 5 paths at 60 GHz. This behavior can be attributed to the shorter wavelength at 80 GHz, which makes the channel more sensitive to small-scale variations in the environment. In contrast, the maximum number of resolvable paths was nearly twice as high at 60 GHz, reaching about 80, whereas at 80 GHz it peaked at only about 40. These differences arise not only from frequency-dependent propagation effects but also from distinct antenna radiation characteristics. In particular, the wider HPBW of the antennas used at 60 GHz enables

the reception of a larger number of MPC.

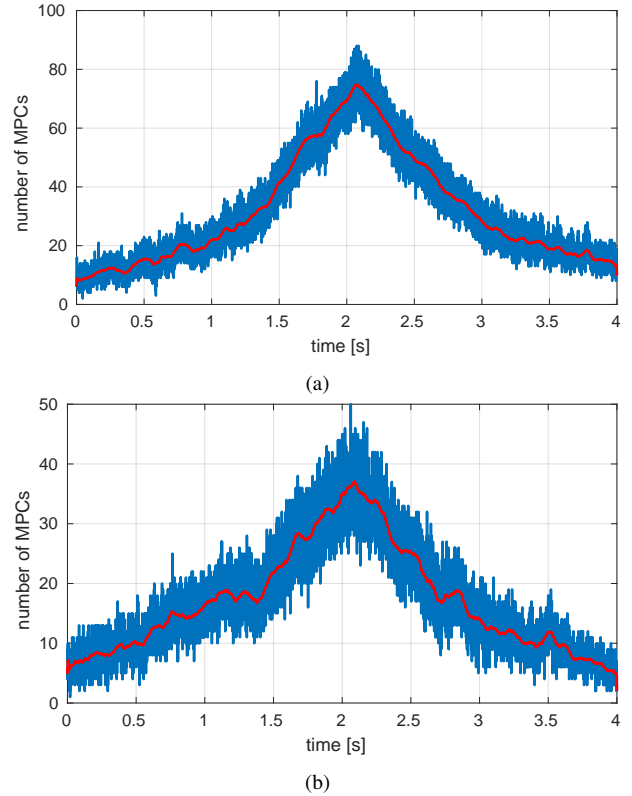


Fig. 7: Number of resolvable propagation paths over time – 60 GHz (a) and 80 GHz (b) bands.

## V. CONCLUSION

The results confirm that the 60 GHz and 80 GHz frequency bands exhibit distinct statistical distributions of the RMS delay spread in the oncoming vehicle scenario, highlighting the frequency-dependent nature of multipath propagation in dynamic vehicular environments. At 60 GHz, the delay spread is well approximated by a Gaussian distribution with a higher median value (19.97 ns), whereas at 80 GHz the distribution follows a lognormal form with a lower median (16.71 ns). These findings indicate that within the MMW spectrum, propagation characteristics cannot be generalized across frequency bands. The analysis of the temporal variation of multipath components further shows that the richness and stability of the channel are strongly dependent on both frequency and antenna characteristics. While the 60 GHz band supports a larger number of resolvable propagation paths, partly due to the wider antenna HPBW, the 80 GHz band is more sensitive to small-scale changes in the environment, resulting in stronger fluctuations around the mean. Future work will focus on extending the analysis to additional vehicular scenarios to provide a more comprehensive understanding of high-frequency vehicular propagation channels.

## ACKNOWLEDGMENT

The research described in this paper was financed by the Czech Science Foundation, Project No. 23-04304L, Multi-band prediction of millimeter-wave propagation effects for dynamic and fixed scenarios in rugged time varying environments and by the Internal Grant Agency of the Brno University of Technology under project no. FEKT-S-23-8191. The work of A. Chandra is supported by the Chips-to-Startup (C2S) program no. EE-9/2/2021-R&D-E from MeitY, GoI. The work of J. Kelner, J. Wojtuń and C. Ziółkowski was funded by the National Science Centre, Poland, under the OPUS-22 (LAP) call in the Weave program, as part of research project no. 2021/43/I/ST7/03294, acronym ‘MubaMilWave’.

## REFERENCES

- [1] A. F. Molisch, F. Tufvesson, J. Karedal, and C. F. Mecklenbrauker, “A survey on vehicle-to-vehicle propagation channels,” *IEEE Wireless Communications*, vol. 16, no. 6, pp. 12–22, 2009.
- [2] C. K. Anjinappa and I. Guvenc, “Millimeter-wave v2x channels: Propagation statistics, beamforming, and blockage,” in *2018 IEEE 88th Vehicular Technology Conference (VTC-Fall)*, 2018, pp. 1–6.
- [3] X. Liu, S. Liu, W. Zhou, L. Yang, and G. Yue, “Measurements and modeling of millimeter-wave vehicle-to-vehicle propagation with vehicle obstructions,” *IEEE Transactions on Wireless Communications*, vol. 24, no. 5, pp. 4024–4039, 2025.
- [4] J. Blumenstein, A. Prokes, J. Vychodil, T. Mikulasek, J. Milos, E. Zöchmann, H. Groll, C. F. Mecklenbräuker, M. Hofer, D. Löschenbrand, L. Bernadó, T. Zemen, S. Sangodoyin, and A. Molisch, “Measured high-resolution power-delay profiles of nonstationary vehicular millimeter wave channels,” in *2018 IEEE 29th Annual International Symposium on Personal, Indoor and Mobile Radio Communications (PIMRC)*, 2018, pp. 1–5.
- [5] A. F. Molisch, C. F. Mecklenbräuker, T. Zemen, A. Prokes, M. Hofer, F. Pasic, and H. Hammoud, “Millimeter-wave v2x channel measurements in urban environments,” *IEEE Open Journal of Vehicular Technology*, vol. 6, pp. 520–541, 2025.
- [6] E. Zochmann, C. F. Mecklenbräuker, M. Lerch, S. Pratschner, M. Hofer, D. Löschenbrand, J. Blumenstein, S. Sangodoyin, G. Artner, S. Caban, T. Zemen, A. Prokeš, M. Rupp, and A. F. Molisch, “Measured delay and doppler profiles of overtaking vehicles at 60 ghz,” in *12th European Conference on Antennas and Propagation (EuCAP 2018)*, 2018, pp. 1–5.
- [7] M. Boban, D. Dupleich, N. Iqbal, J. Luo, C. Schneider, R. Müller, Z. Yu, D. Steer, T. Jämsä, J. Li, and R. S. Thomä, “Multi-band vehicle-to-vehicle channel characterization in the presence of vehicle blockage,” *IEEE Access*, vol. 7, pp. 9724–9735, 2019.
- [8] Z. Zhang, R. He, B. Ai, M. Yang, X. Zhang, Z. Qi, and Y. Yuan, “Channel measurements and modeling for dynamic vehicular isac scenarios at 28 ghz,” *IEEE Transactions on Communications*, vol. 73, no. 8, pp. 6884–6897, 2025.
- [9] R. Zavorka, T. Mikulasek, J. Vychodil, J. Blumenstein, A. Chandra, H. Hammoud, J. M. Kelner, C. Ziółkowski, T. Zemen, C. Mecklenbräuker, and A. Prokes, “Characterizing the 80 ghz channel in static scenarios: Diffuse reflection, scattering, and transmission through trees under varying weather conditions,” *IEEE Access*, vol. 12, pp. 144 738–144 749, 2024.